Islamic Azad University

Journal of
Optoelectronical Nanostructures

Winter 2021 / Vol. 7, No. 1

Research Paper

Giant Enhancement of Second Harmonic Generation Efficiency from Monolayer Group-VI Transition Metal Dichalcogenides (*WS_2 and WSe_2*) Embedded in 1D Photonic Crystals

Samira Bahrami[1], Omid Bahrami[1]

[1] Department of physics, Farhangian university, Tehran

Received: 24 Dec. 2021
Revised: 18 Jan. 2022
Accepted: 15 Feb. 2022
Published: 5 Mar. 2022

Use your device to scan and read the article online

Keywords:
Transition Metal Dichalcogenide, SH Generation, Transfer Matrix Method

Abstract: In this study, an effective numerical method was used to describe NLO impacts on photonic crystal structures, particularly 2D TMDCs and three-dimensional (3D) materials (air and SiO_2). Moreover, the amplification of the second harmonic (SH) efficiency in one-dimensional (1D) photonic crystals, including TMDCs, was investigated. These photonic crystal structures comprise of air, SiO_2, and TMDC layers that are periodically arranged; however, the first two layers have the same thickness. The transfer matrix method was applied to calculate the SH efficiency and no-reduction field approximation. The incident wavelength λ of 810 nm was achieved by adjusting the thickness of the air and SiO_2 layers. In addition, by choosing a specific thickness, the harmonic waves generated in the structure interacted constructively. The conditions were such that both the fundamental and the SH waves lay in the edge of the band gap, where the density of electromagnetic modes and interaction time increased. However, density of electromagnetic modes and interaction time interaction enhanced the efficiency of the SH efficiency.

Citation: Bahrami S, Bahrami O. Giant enhancement of second harmonic generation efficiency from monolayer group-VI transition metal dichalcogenides (*WS_2 and WSe_2*) embedded in 1D photonic crystals.
Journal of Optoelectronical Nanostructures (JOPN). 2022; 7 (1): 67- 96.
DOI: 10.30495/JOPN.2022.28839.1234

***Corresponding author:** Samira Bahrami
Address: Department of Physics, Farhangian University, Tehran, Iran.
Tell: 00989173027100 **mail:** samira_bahrami@cfu.ac.ir

1. INTRODUCTION

The use of two-dimensional (2D) materials such as graphene and transition metal dichalcogenides (TMDCs) in multilayer structures has received many attentions over the past few years [1-4]. Recently, TMDCs have attracted a lot of interests owing to their electrical and optical attributes, particularly band gap, that are highly dependent on the width of the layer [3, 4]. As an example, volumetric TMDCs have indirect band gaps, while their single-layer type has direct band gaps ranging from 1.55 to 1.9 eV [3, 5, 6], which causes monolayer TMDCs (ML-TMDCs) to be used in modulators and light-emitting devices [4, 7]. ML-TMDCs comprise of two hexagonal lattices of chalcogen atoms separated by a sheet of metallic atoms sandwiched between the chalcogens in a trigonal prismatic arrangement [5]. Structurally, these materials are non-centrosymmetric if the number of the layers is odd, but they are centrosymmetric in case of even layer number or volumetric TMDCs [8]. The non-centrosymmetric feature makes these 2D materials have a significant second-order susceptibility $\chi^{(2)}$.

Nonlinear optical (NLO) processes, including frequency conversion, optical signal processing, ultrafast pulses, and parametric sources of quantum state, play a significant role in 2D materials, which have a broad application in integrated photonics circuits [9–14]. NLO response of 2D materials in waveguides [9,15] and multilayer structures gives rise to the amplification of wave packets when passing [9,10]. So far, research on TMDCs has been focused on electronic features and linear optics, and very few studies have investigated the NLO properties of these materials. Furthermore, surveys on the second harmonic generation (SHG) have mostly been conducted on MoS_2 [8, 16-18], $MoSe_2$ [19], WS_2 [20], and WSe_2 [21] in monolayer and trilayer forms.

With the aim of enhancing the efficiency of SHG in one-dimensional (1D) multilayer structures containing TMDC monolayers Ws_2 and Wse_2, we conducted this study. A 1D multilayer structure, i.e. photonic crystal, consists of at least two layers (with different refractive indexes) arranged periodically. As the motion of an electron in solid-state physics is influenced by a multilayer structure, in photonic crystal, the photon motion is affected by the multilayer structure of these crystals [26–28]. External feedback, defective mode, and quasi-phase matching are several mechanisms contribute to the enhancement of the SHG in photonic crystals [22–25]. In the present work, we utilized the quasi-phase matching technique and transfer matrix method (TMM) to enhance the efficiency of SHG in TMDC layers Ws_2 and Wse_2 by altering the thickness of dielectric materials used in 1D multilayer structures [22–25].

2. STRUCTURE OF MONOLAYRE TMDCs, MODEL, AND METHOD

TMDCs are a bunch of materials with the chemical formula MX_2, where M is a transition metal from group 4 to 10 of the periodic table, and X represents chalcogen elements in group 16 of the periodic table consisting of sulfur (S), selenium (Se), and tellurium (Te) (Fig. 1).

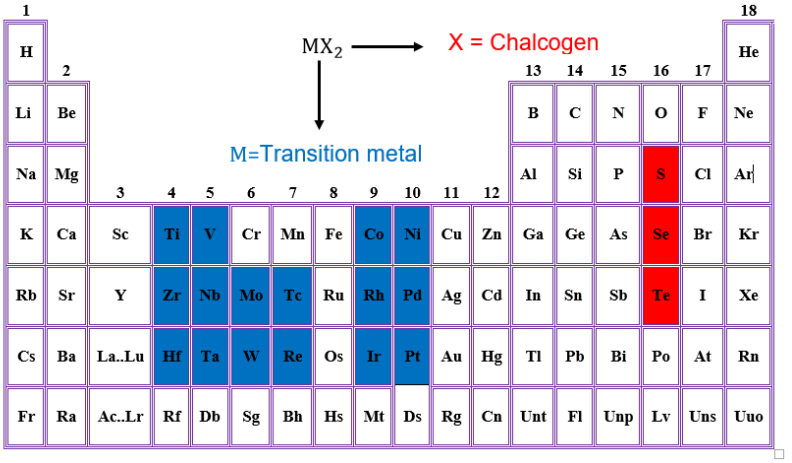

Fig. 1. Periodic table. Blue and red colors indicate the transition metals and chalcogens, respectively [29].

The TMDC structure in Figure 2 displays a transition layer of metal between two layers of chalcogens.

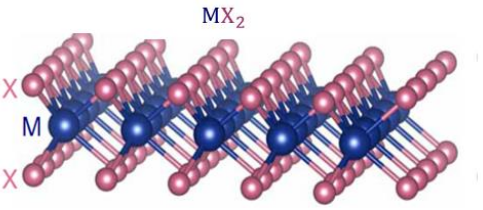

Fig. 2. Structure of TMDC [30]. M, transition metals; X, chalcogens

Since the physical structure of 2D TMDCs consists a single atomic layer, their electromagnetic properties are described by surface quantities. For instance, the conductivity of these 2D materials is expressed as σ_s, where s implies the surface. In numerical methods, the use of bulk quantities is easier than surface quantities. As an example, instead of surface conductivity σ_s, bulk conductivity $\sigma_b = \frac{\sigma_s}{h_{eff}}$ is used, where h_{eff} is the effective thickness of the 2D materials. The electric permittivity ε in the 2D materials is calculated as follows:

$$\varepsilon(\omega) = \varepsilon_0(1+\frac{i\sigma_b}{\varepsilon_0\omega}) = \varepsilon_0(1+\frac{i\sigma_s}{\varepsilon_0\omega\, h_{eff}}) \quad (1)$$

In case of 2D TMDCs, the relative permittivity $\varepsilon_r(\omega) = \frac{\varepsilon(\omega)}{\varepsilon_0}$ is expressed as a superposition of N Lorentzian functions:

$$\varepsilon_r(\omega) = \frac{\varepsilon(\omega)}{\varepsilon_0} = 1+\sum_{k=1}^{N}\frac{f_k}{\omega_k^2-\omega^2-i\gamma_k\omega} \quad (2)$$

Where f_k, ω_k, and γ_k are the oscillator strength, resonance frequency, and spectral width of the k_{th} oscillator, respectively. The values of these parameters for the two 2D TMDCs examined in this study are shown in Table 1 in terms of $E_k = \hbar\omega_k$, $f_k^E = \hbar^2 f_k$, , and $\gamma_k^E = \hbar\gamma_k$ [31].

TABLE I
MODEL PARAMETERS FOR THE RELATIVE PERMITTIVITY OF TWO TMDC MONOLAYER MATERILAS PARAMERERIZED BY THE MULTI-LORENTIZIAN DISPERSION RELATION DEFINED BY Eq. (2).

	WS_2			WSe_2		
h_{eff}	6.18 Å			6.49 Å		
k	$E_k(eV)$	$f_k^E(eV^2)$	$\gamma_k^E(eV)$	$E_k(eV)$	$f_k^E(eV^2)$	$\gamma_k^E(eV)$
1	2.009	1.928	0.032	1.654	0.557	0.036
2	2.204	0.197	0.250	2.426	5.683	0.243
3	2.198	0.176	0.161	2.062	1.036	0.115
4	2.407	0.142	0.112	2.887	16.11	0.344
5	2.400	2.980	0.167	2.200	1.500	0.300
6	2.595	0.540	0.213	2.600	1.500	0.300
7	2.644	0.050	0.171	3.800	70.00	0.700
8	2.831	12.60	0.266	5.000	80.00	0.700
9	3.056	8.765	0.240	-	-	-
10	3.577	29.99	1.196	-	-	-
11	5.078	49.99	1.900	-	-	-
12	5.594	79.99	2.510	-	-	-

Extinction coefficient and the refractive index of the TMDC monolayer materials are obtained from the complex permittivity as follows:

$$\eta_M(\omega) = \sqrt{\frac{1}{2}(\varepsilon_{rM} + \sqrt{\varepsilon_{rM}^2 + \varepsilon_{iM}^2})}$$

$$K_M(\omega) = \sqrt{\frac{1}{2}(-\varepsilon_{rM} + \sqrt{\varepsilon_{rM}^2 + \varepsilon_{iM}^2})} \quad (3)$$

Since SiO_2 is used in the structure, its refractive index is calculated using the following formula [32]:

$$\eta_S(\lambda) = \sqrt{A + \frac{B\lambda^2}{\lambda^2 - C} + \frac{D\lambda^2}{\lambda^2 - 100}} \quad (4)$$

where A = 1.28604141, B = 1.07044083, C = 1.00585997 × 10^{-2}, D = 1.10202242, and λ is in nm unit [32]. The refractive index of air layers was set to be equal to one.

In the structure under study, we assume that the interface between the layers is located at the x-y plane (Fig. 3), and the fundamental waves (FW) of wavelength λ and the polarization of the electric field are in the x-axis direction. In other words, these waves vertically incident on the surface of the nonlinear multilayer structure and propagate in the z-axis direction

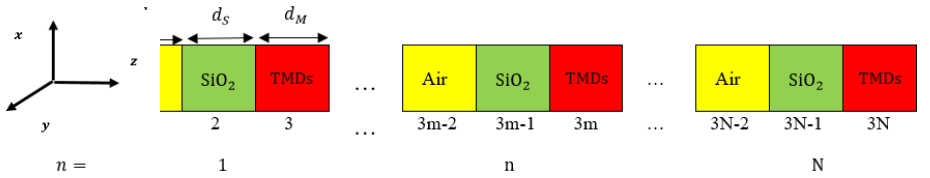

Fig. 3. Finite 1D photonic crystal arrangement.

The second-order nonlinear susceptibility tensor has nonzero elements of $\chi^{(2)}_{y'y'y'} = -\chi^{(2)}_{y'x'x'} = -\chi^{(2)}_{x'x'y'} = -\chi^{(2)}_{x'y'x'}$, where x', y', and z' are crystalline coordinates. x' is along the armchair direction (Fig. 4). In our 1D photonic crystal structure, the incident beam is linearly polarized light along the x-axis direction where the *x*, *y*, and *z* directions are shown in Figure 3 and referred to as lab coordinates.

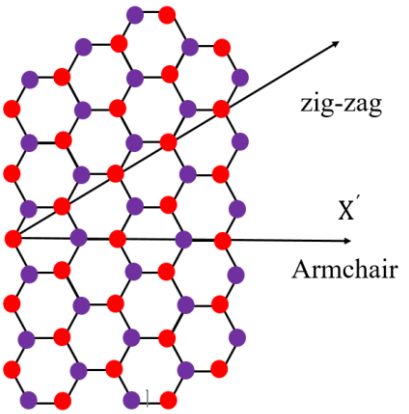

Fig. 4. Lattice structure of TMDC monolayer. Purple and red circles indicate dichalcogenide atoms and transition metal atoms, respectively.

In undepleted pump approximation, the electric field of the FW $E_m^{(f)}(z)$ and that of the SH wave, $E_m^{(s)}(z)$, in the m th layer are measured by the aid of the following equations [22–25]:

$$[\frac{d^2}{dz^2}+(k_m^f)^2]E_m^f(z)=0$$
$$[\frac{d^2}{dz^2}+(k_m^s)^2]E_m^s(z)=-\mu_0(2\omega)^2\vec{P}_{NL}^{2\omega} \quad (5)$$

Where $k_m^{(f)}=n_m^{(f)}k_0^{(f)}, k_m^{(s)}=n_m^{(s)}k_0^{(s)}, k_0^{(f)}=\frac{\omega}{C}, k_0^{(s)}=\frac{2\omega}{C}$, as well as $n_m^{(f)}$ and $n_m^{(s)}$ respectively show the refractive index of the pump waves and the SH in the m th slab. C indicates the speed of light is in vacuum. The first equation of coupling equations (5) gives the fundamental electric field in the m th layer.

$$E_m^f(z)=E_m^{f+}e^{i(k_m^f(z_m-z_{m-1})-\omega t)}+E_m^{f-}e^{-i(k_m^f(z_m-z_{m-1})-\omega t)} \quad (6)$$

Where $z_0=0$, $z_m=z_{m-1}+d_m$, and d_m denotes the thickness of the m th layer. Also, E_m^{f+} and E_m^{f-} are the magnitude of forward and backward plane waves at the left interface of the m th layer.

Based on the structure studied herein, for structures containing three types of layers, the amplitude of forward and backward FW electric field in each layer is achieved using the boundary conditions as follows:

$$\begin{pmatrix} E_{3m-2}^{f+} \\ E_{3m-2}^{f-} \end{pmatrix} = D_A^{-1} t^{m-1} D_0 \begin{pmatrix} E_0^{f+} \\ E_0^{f-} \end{pmatrix}$$

$$\begin{pmatrix} E_{3m-1}^{f+} \\ E_{3m-1}^{f-} \end{pmatrix} = D_s^{-1} D_A P_A D_A^{-1} t^{m-1} D_0 \begin{pmatrix} E_0^{f+} \\ E_0^{f-} \end{pmatrix} \quad (7)$$

$$\begin{pmatrix} E_{3m}^{f+} \\ E_{3m}^{f-} \end{pmatrix} = D_{TMDC}^{-1} D_s P_s D_s^{-1} D_A P_A D_A^{-1} t^{m-1} D_0 \begin{pmatrix} E_0^{f+} \\ E_0^{f-} \end{pmatrix}$$

Where:

$$D_m = \begin{pmatrix} 1 & 1 \\ n_m^f & -n_m^f \end{pmatrix} \quad (8)$$

$$P_m = \begin{pmatrix} e^{ik_m^f d_m} & 0 \\ 0 & e^{-ik_m^f d_m} \end{pmatrix} \qquad m = A, S, TMDC, 0$$

$E_{3m-k}^{f\pm}$ with k = 0, 1, and 2 represents the forward and backward FW electric field amplitudes at the left-hand side of layers for TMDC ($k=0$), SiO_2 ($k=1$), and air ($k=2$) in m th segment, respectively (Fig. 3). The subscripts A, S, TMDC, and 0 refer to the air, SiO_2, TMDC, and background medium, respectively. t is the transfer matrix of one period consisting of three layers of air, SiO_2, and TMDC.

$$t = D_{TMDC} P_{TMDC} D_{TMDC}^{-1} D_s P_s D_s^{-1} D_A P_A D_A^{-1} \quad (9)$$

Following the calculation of the fundamental electric fields, we can calculate the SH electric fields. Inserting the FW solution (eq. (6)) into eq. (5), we can acquire the amplitude of SH electric field in m th layer as follows:

$$E_m^s(z) = E_m^{s+} e^{ik_m^s (z-z_{m-1})} + E_m^{s-} e^{-ik_m^s (z-z_{m-1})} + A_m (E_m^{f+})^2 e^{2ik_m^f (z-z_{m-1})} + A_m (E_m^{f-})^2 e^{-2ik_m^f (z-z_{m-1})} + C_m E_m^{f+} E_m^{f-} \quad (10)$$

Where $E_i^{s\pm}$ are forward and backward SH electric field amplitudes, respectively, at the left-hand side of the m th layer [22-25]

$$C_m = -\frac{2(k_0^s)^2 \chi_m^s}{(k_m^s)^2}, A_m = -\frac{(k_0^s)^2 \chi_m^s}{(k_m^s)^2 - 4(k_m^f)^2} \quad (11)$$

We used the Maxwell's equation as $\vec{\nabla} \times \vec{E}_m^s = ik_0^s \vec{H}_m^s(z)$ and acquired the SH magnetic field, as indicated in the following equation.

$$H_m^s(z) = n_m^s (E_m^{s+} e^{ik_m^s (z-z_{m-1})} + E_m^{s-} e^{-ik_m^s (z-z_{m-1})}) + n_m^f (A_m (E_m^{f+})^2 e^{2ik_m^f (z-z_{m-1})} + A_m (E_m^{f-})^2 e^{-2ik_m^f (z-z_{m-1})}) \quad (12)$$

Applying boundary conditions for SH electric and magnetic fields, we can write the forward and backward SH electric field amplitudes at the (m −1) th and m th layers as

$$\begin{pmatrix} E_m^{s+} \\ E_m^{s-} \end{pmatrix} = t_m^{(s)} \begin{pmatrix} E_{m-1}^{s+} \\ E_{m-1}^{s-} \end{pmatrix} + \begin{pmatrix} r_m^+ \\ r_m^- \end{pmatrix} \quad (13)$$

Where

$$t_m^s = G_0 N_m G_0^{-1}, \qquad N_m = G_m Q_m G_m^{-1} \quad (14)$$

$$\begin{pmatrix} r_m^+ \\ r_m^- \end{pmatrix} = G_0^{-1}(B_m F_m - N_m B_m) A_m \times \begin{pmatrix} (E_m^{f+})^2 \\ (E_m^{f-})^2 \end{pmatrix} + (1 - N_m) C_m \begin{pmatrix} E_m^{f+} E_m^{f-} \\ 0 \end{pmatrix} \quad (15)$$

And

$$G_0 = \begin{pmatrix} 1 & 1 \\ n_0 & -n_0 \end{pmatrix}, G_m = \begin{pmatrix} 1 & 1 \\ n_m^s & -n_m^s \end{pmatrix}, B_m = \begin{pmatrix} 1 & 1 \\ 2n_m^f & -2n_m^f \end{pmatrix} \quad (16)$$

$$Q_m = \begin{pmatrix} e^{ik_m^s d_m} & 0 \\ 0 & e^{-ik_m^s d_m} \end{pmatrix} \quad (17)$$

$$F_m = \begin{pmatrix} e^{2ik_m^f d_m} & 0 \\ 0 & e^{-2ik_m^f d_m} \end{pmatrix} \quad (18)$$

Using the high recurrence relation, we can achieve the SH electric field in the n th segment based on the n-1 th segment as follows:

$$\begin{aligned} \begin{pmatrix} E_n^{s+} \\ E_n^{s-} \end{pmatrix} &= G_0^{-1} S_3 G_0 \begin{pmatrix} E_{n-1}^{f+} \\ E_{n-1}^{f-} \end{pmatrix} + G_0^{-1}[(S_2 B_A F_A - S_3 B_A) A_A \begin{pmatrix} E_{3n-2}^{f+} \\ E_{3n-2}^{f-} \end{pmatrix} \\ &+ (S_2 - S_3) C_A \begin{pmatrix} E_{3n-2}^{f+} E_{3n-2}^{f-} \\ 0 \end{pmatrix} + (S_1 B_s F_s - S_2 B_s) A_s \begin{pmatrix} E_{3n-1}^{f+} \\ E_{3n-1}^{f-} \end{pmatrix} \\ &+ (S_1 - S_2) C_s \begin{pmatrix} E_{3n-1}^{f+} E_{3n-1}^{f-} \\ 0 \end{pmatrix} + (B_{TMDC} F_{TMDC} - S_1 B_{TMDC}) A_{TMDC} \begin{pmatrix} E_{3n}^{f+} \\ E_{3n}^{f-} \end{pmatrix} \\ &+ (1 - S_1) C_{TMDC} \begin{pmatrix} E_{3n-2}^{f+} E_{3n-2}^{f-} \\ 0 \end{pmatrix}] \end{aligned} \quad (19)$$

where $S_1 = N_{TMDC}$, $S_2 = N_{TMDC} N_S$, and $S_3 = N_{TMDC} N_S N_A$. We disregard the nonlinear behavior of air and silicon layers with respect to the TMDC monolayers ($\chi_A^{(s)} \cong 0$, $\chi_s^{(s)} \cong 0$). The SH electric fields at the two ends of the structure were obtained as follows:

$$\begin{pmatrix} E_t^{s+} \\ 0 \end{pmatrix} = G_0^{-1} S_3^N G_0 \begin{pmatrix} 0 \\ E_r^{s-} \end{pmatrix} + \sum_{n=1}^{N} G_0^{-1} S_3^{N-n} [(B_{TMDC} F_{TMDC} - S_1 B_{TMDC}) A_{TMDC} \begin{pmatrix} E_{3n}^{f+} \\ E_{3n}^{f-} \end{pmatrix} + (1 - S_1) C_{TMDC} \begin{pmatrix} E_{3n}^{f+} E_{3n}^{f-} \\ 0 \end{pmatrix}] \quad (20)$$

Where $E_t^{(s)+}$ and $E_r^{(s)-}$ denote forward and backward SH electric fields, respectively. Forward and backward SHG efficiencies were defined as follows:

$$\eta_B = \frac{\left|E_r^{s-}\right|^2}{\left|E_0^f\right|^2}, \quad \eta_F = \frac{\left|E_t^{s+}\right|^2}{\left|E_0^f\right|^2} \quad (21)$$

3. NUMERICAL RESULTS

In the numerical calculations below, the incident wavelength is 810 nm. We assume that air and SiO_2 layers have similar thickness ($d_A = d_s = d$), which can be altered in simulations. However, the thickness of TMDC monolayers was fixed at $d_{WS_2} = 61.8\ nm$ and $d_{WSe_2} = 64.9\ nm$. The second-order susceptibility of TMDC monolayers was set as $\chi^{(2)}_{WS_2} = 16.2 \times 10^{-9} \frac{m}{V}$ and $\chi^{(2)}_{WSe_2} = 16.5 \times 10^{-9} \frac{m}{V}$. We disregarded the nonlinear behavior of air and silicon layers relative to the TMDC monolayers ($\chi_A^{(S)} \cong 0, \chi_s^{(S)} \cong 0$) [10,11].

Figure 5 shows the calculated forward and backward SHG efficiencies versus the same thickness of air and SiO_2 layers, changing from 200 to 2000 nm, for multilayer structures composed of WS_2, WSe_2, containing 35 segments.

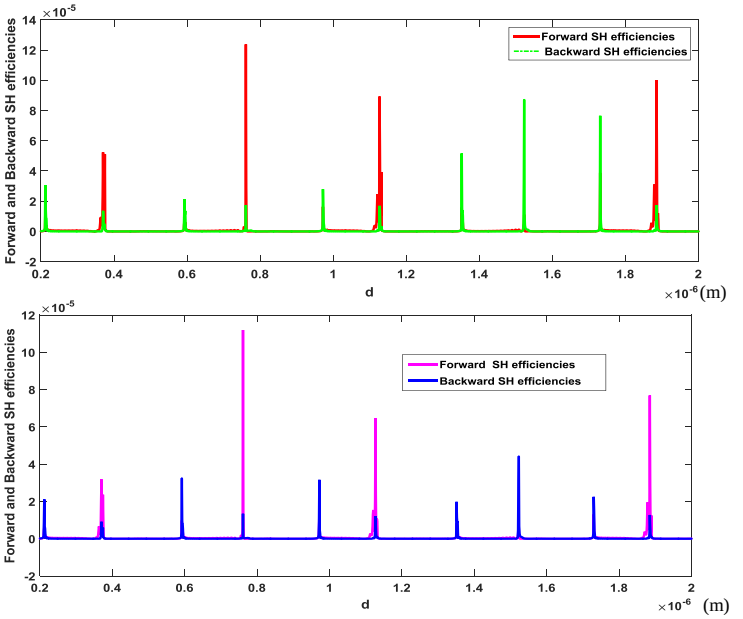

Fig. 5. Forward and backward SHG efficiencies versus the same thickness of air and SiO_2 layers for multilayer structure composed of Ws_2 (up) and WSe_2 (down), containing 35 segments.

As shown in the Figure, the SHG efficiencies increase in some thicknesses. The maximum forward and backward efficiencies are $\eta_F = 12.378\times10^{-5}$ and $\eta_B = 8.6922\times10^{-5}$ for Ws_2 and $\eta_F = 5.3452\times10^{-5}$ and $\eta_B = 3.6743\times10^{-5}$ for WSe_2. Besides, the maximum η_F and η_B for Ws_2 occur when $d_A = d_s = 761.00nm$ and $d_A = d_s = 1523.0nm$, while for WSe_2, the maximum η_F and η_B happen at $d_A = d_s = 761.00nm$ $d_A = d_s = 971.00nm$, respectively.

As stated above, the layers of TMDC monolayers in the multilayer structures, i.e. those we applied in our study, are the SH wave source. It means that harmonic waves produce in different layers and interact with each other. As we know, if the phase difference between waves is an integer multiple of the SH wavelength, then the interference of the SH waves is constructive ($\Delta\phi = n\lambda^{(\frac{1}{2})}$ where n is an integer, and $\lambda^{(\frac{1}{2})}$ is SH wavelength).

The main factor of this phase difference is the optical path difference of the SH wave between the TMDC monolayers in the multilayered structure and equals $l_{op} \approx (n_A + n_s(\lambda))d$. If we ignore the length of the optical path in the TMDC monolayers (nonlinear sources), which is infinitely small, the optical path length for maximum efficiencies is $l_{op} \approx 9\lambda^{(\frac{1}{2})}$, where $\lambda^{(\frac{1}{2})} = 405nm$. The disagreement between maximum efficiencies is due to the effect of the optical path length in the TMDC monolayer, which affects the interference of SH waves.
In the next phase of our study, we compared and examined the SHG efficiencies in multilayer structures, i.e. WS_2, containing different numbers of segments. Figure 6 and Table 2 illustrate the results of forward and backward efficiencies and optimum thickness of forward and backward SH waves for N = 1, 10, 20, 30, 40, and 50 segments near $d = d_A = d_{SiO_2} = 750nm$.

Table II
The maximum forward and backward efficiencies and optimum thickness of air and SiO_2 for forward and backward SH waves for several segments of WS_2

N	η_F	η_B	$d_F(nm)$	$d_B(nm)$
1	6.9677×10^{-9}	6.1872×10^{-9}	740.90	842.60
10	1.7969×10^{-6}	2.5327×10^{-7}	746.50	771.40
20	1.9077×10^{-5}	1.9948×10^{-6}	757.40	757.70
30	9.4087×10^{-5}	9.8039×10^{-6}	760.30	760.30
40	3.1519×10^{-4}	2.6282×10^{-5}	761.50	761.40
50	7.7916×10^{-4}	4.1206×10^{-5}	762.10	762.00

The results demonstrates the maximum enhancement of SHG efficiencies up to three orders of magnitude in 1D photonic crystals containing sub wavelength WS_2 monolayers (including N=10 segments) and about five orders of magnitude for N = 40 segments with respect to N=1 for forward efficiencies. Besides, two orders of magnitude in 1D photonic crystals contains sub wavelength WS_2 monolayers including N=10 segments and about four order of magnitude for N=40 segments with respect to N=1 for backward efficiencies. The results were achieved by tuning the thickness of air and SiO_2 layers to meet the phase matching conditions.

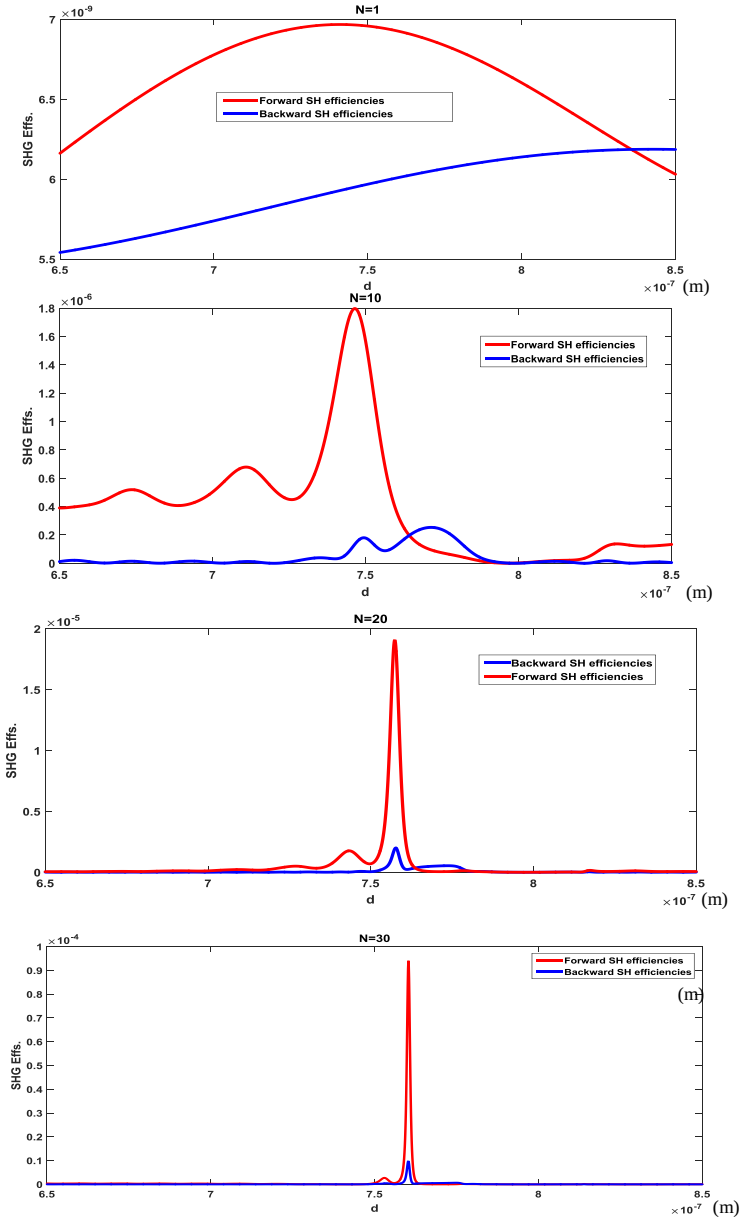

Fig. 6. Forward and backward SHG efficiencies versus the same thickness of air and SiO_2 layers for 1DNPC composed of WS_2 containing N = 1, N = 10, N = 20, N = 30 segments.

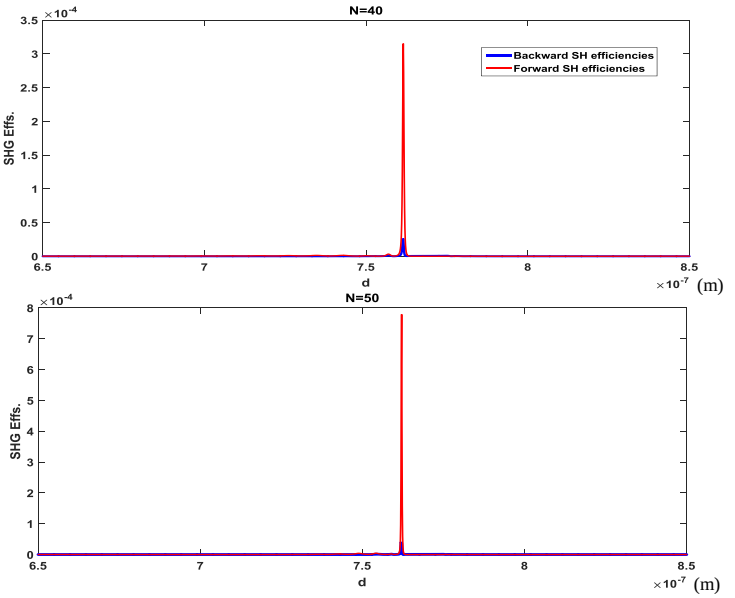

Fig. 7. Forward and backward SHG efficiencies versus the same thickness of air and SiO_2 layers for 1DNPC composed of WS_2 containing N = 40, and N = 50 segments.

For 1DNPC composed of WSe_2 containing different numbers of segments, we compared the SHG efficiencies and obtained the optimum thickness of air and SiO_2 for forward and backward SH waves in the structure comprising of different segments of 1D photonic crystals (Table 3 and Fig. 6,7)

Table III
The maximum forward and backward efficiencies and optimum thickness forward and backward SH waves for several segment of WSe_2

N	η_F	η_B	$d_F(nm)$	$d_B(nm)$
1	5.7660×10^{-9}	4.9441×10^{-9}	1455.0	1559.3
20	9.0886×10^{-6}	3.0723×10^{-6}	1518.3	1519.9
23	1.2054×10^{-5}	7.9613×10^{-6}	1519.6	1520.4
24	1.2718×10^{-5}	1.0651×10^{-5}	1519.9	1520.6
25	1.3121×10^{-5}	1.3962×10^{-5}	1520.3	1520.8
26	1.3284×10^{-5}	1.7909×10^{-5}	1520.6	1521.0

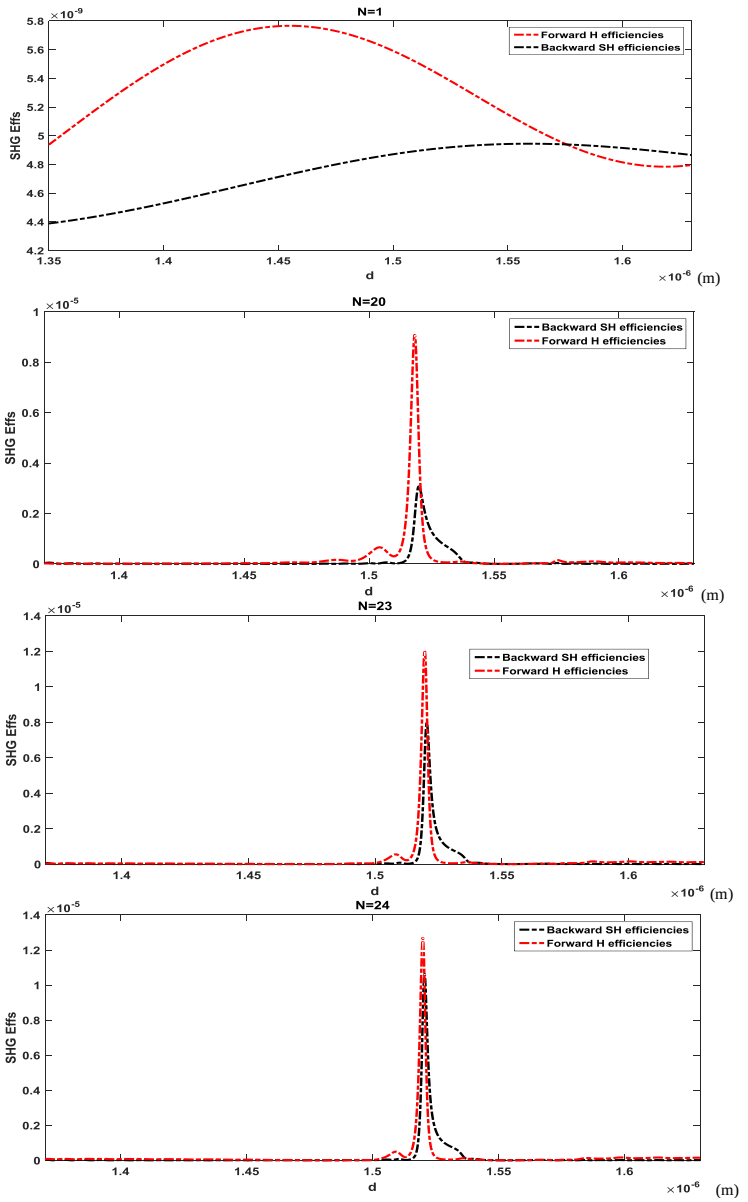

Fig. 8. Forward and backward SHG efficiencies versus the same thickness of air and SiO_2 layers for 1DNPC composed of WSe_2 containing N = 1, N = 20, N = 23, N = 24 segments

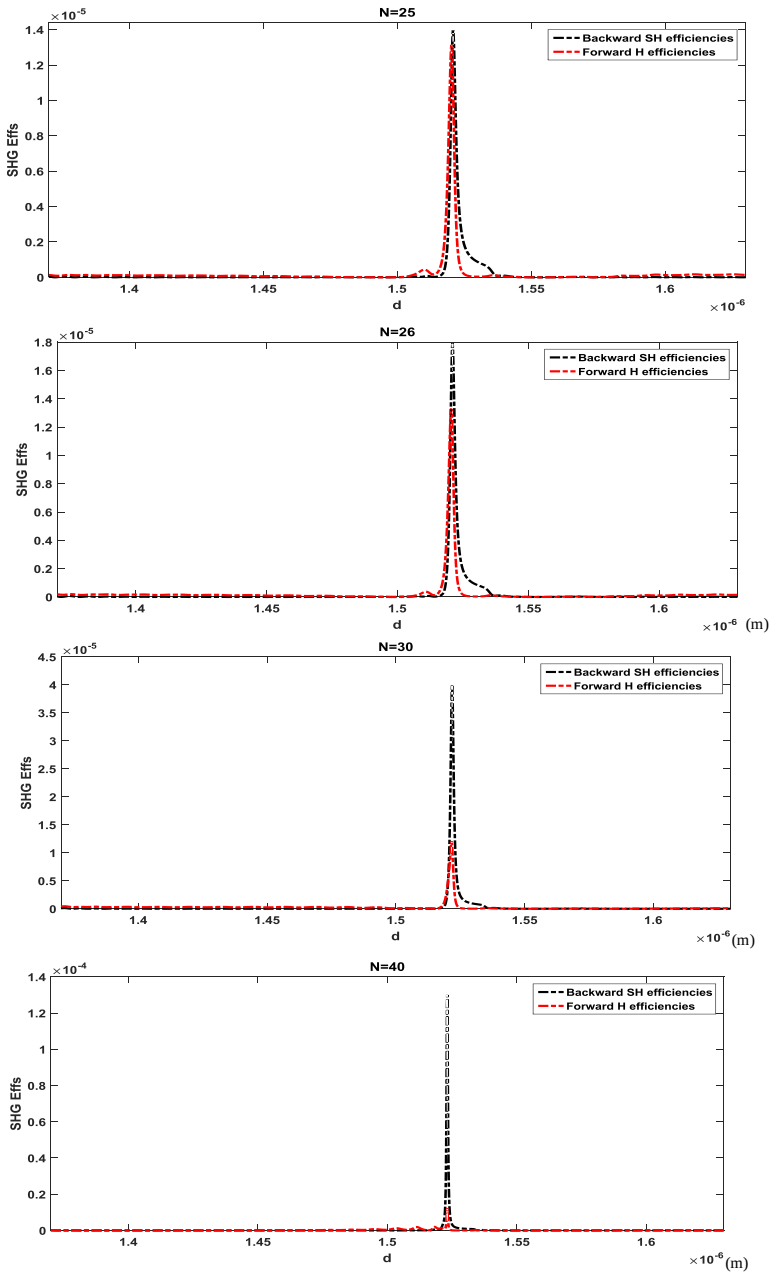

Fig. 9. Forward and backward SHG efficiencies versus the same thickness of air and SiO_2 layers for 1DNPC composed of WSe_2 containing N = 25, and N = 26 N=30 , N=40 segments

The results show the maximum enhancement of SHG efficiencies up to three orders and three orders of magnitude in 1D photonic crystals contains sub wavelength WSe_2 monolayers, including N = 20 segments. Additionally, it contains about four order and five order of magnitude for N = 40 segments with respect to N = 1 for forward and backward efficiencies, respectively. For 1DNPC comprising of WS_2 and WSe_2, to further understand the physics behind the enhancement of the SH efficiencies, the transmission spectra of different engineered structures around the FW and SH wavelength are demonstrated in Figures 10-18. The Figures display that both FW and SH waves are located at the photonic band gap edges for all engineered structures where the density of electromagnetic fields and the group velocity is large and low, respectively [33, 34]. As a result, the field amplitudes can be enhanced, and the nonlinear interaction time becomes much larger.

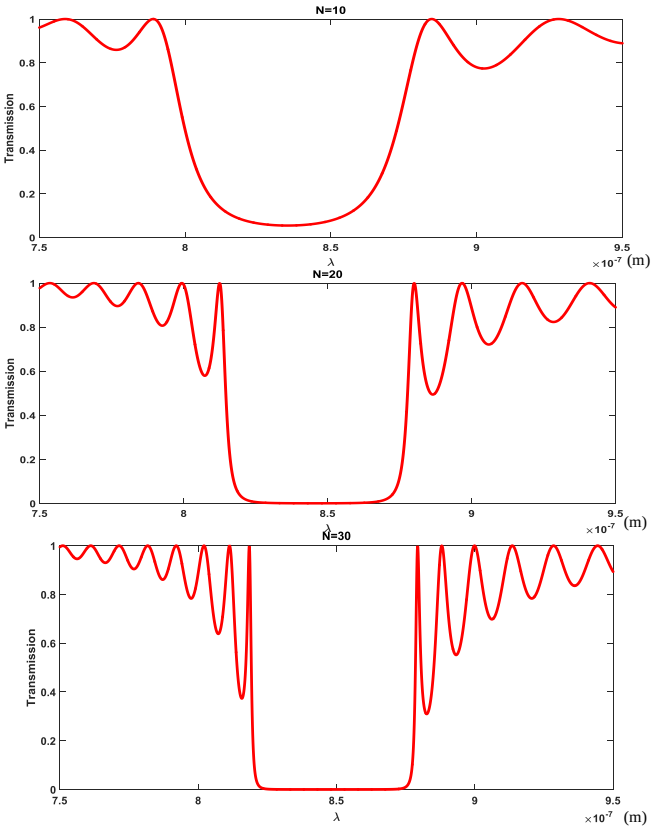

Fig. 10. Transmission spectra around the FW wavelength in 1DNPC composed of WS_2 containing N = 10, N = 20, N = 30 segments.

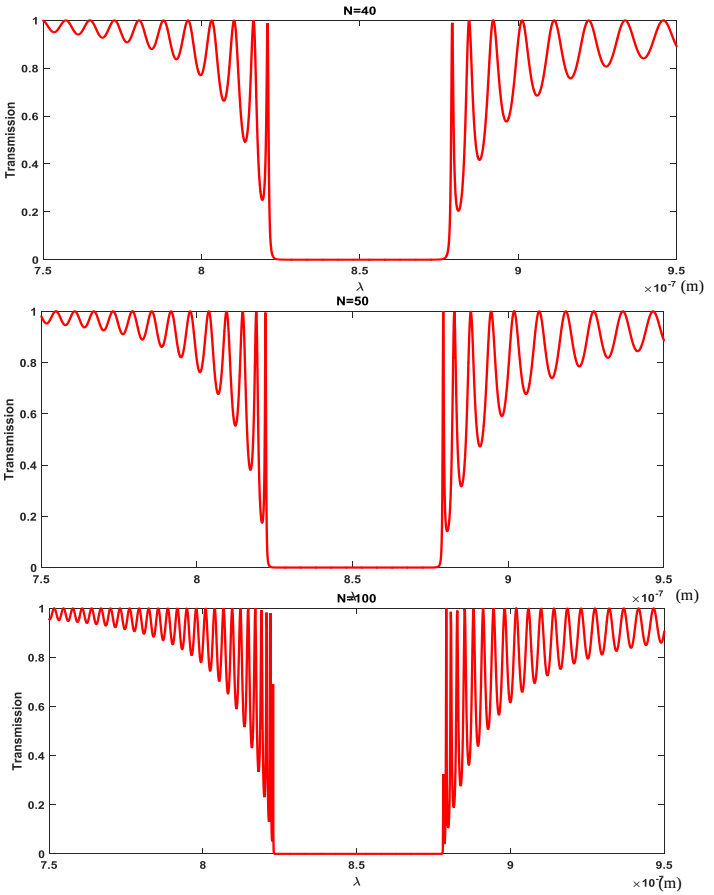

Fig. 11. Transmission spectra around the FW wavelength in 1DNPC composed of WS_2 containing N = 40, N = 50, N = 100 segments.

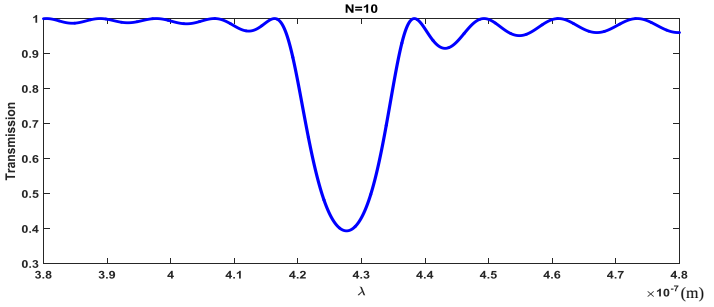

Fig. 12. Transmission spectra around the SH wavelength in 1DNPC composed of WS_2 containing N = 10 segments.

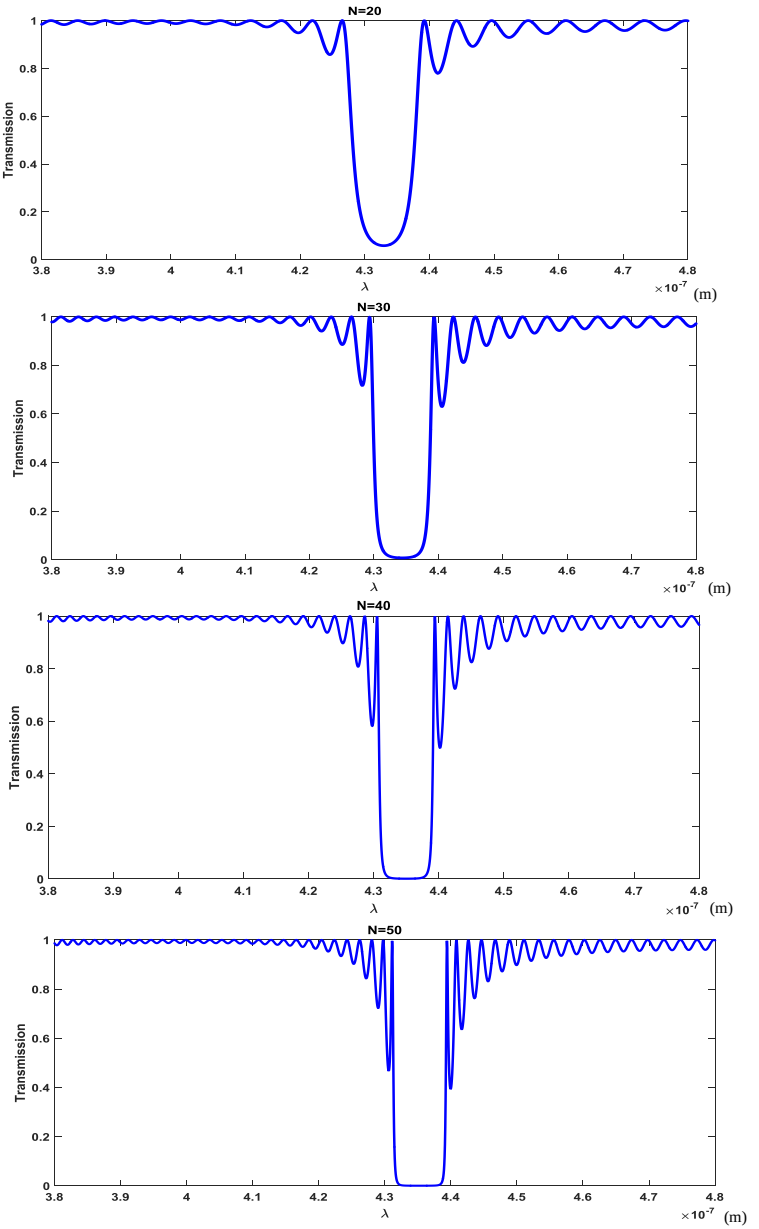

Fig. 13. Transmission spectra around the SH wavelength in 1DNPC composed of WS_2 containing N = 20, 30, 40, 50 segments.

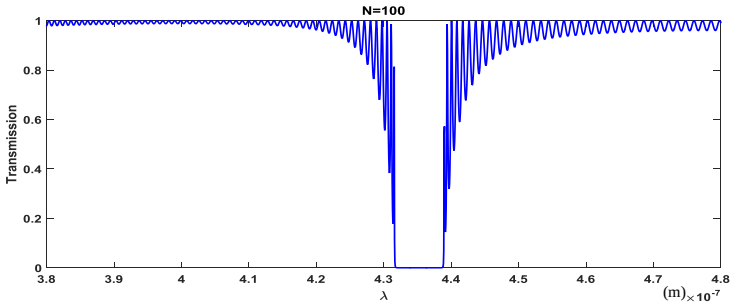

Fig. 14. Transmission spectra around the SH wavelength in 1DNPC composed of WS_2 containing N = 100 segments.

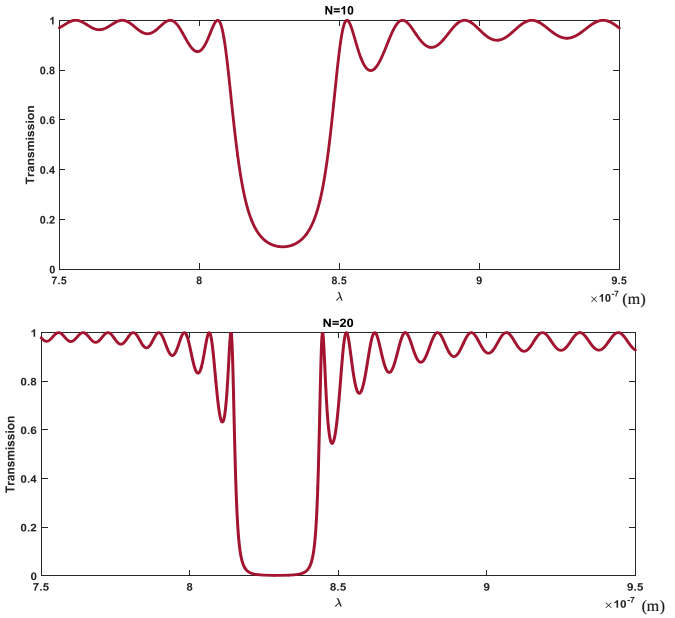

Fig. 15. Transmission spectra around the FW wavelength in 1DNPC composed of WSe_2 contains: N = 10, N = 20 segments.

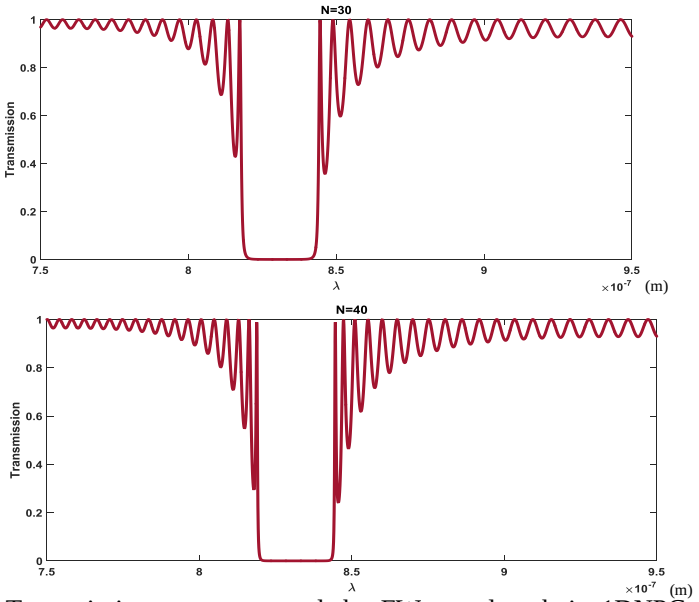

Fig. 16. Transmission spectra around the FW wavelength in 1DNPC composed of WSe_2 contains: N = 30, N = 40 segments.

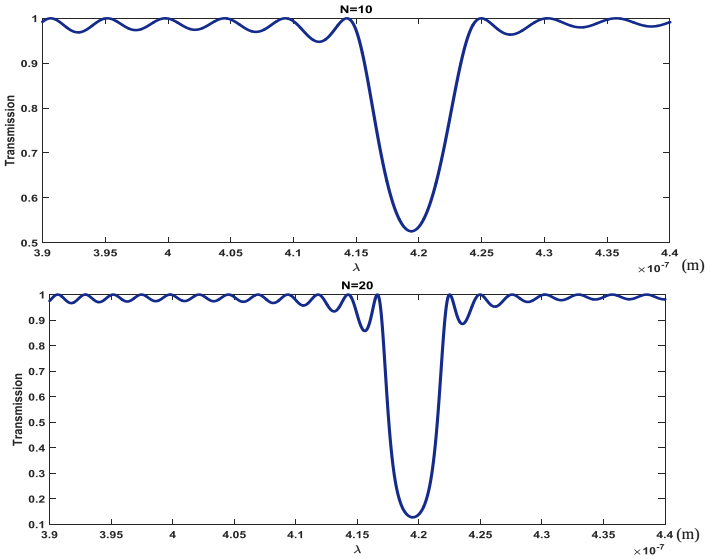

Fig. 17. Transmission spectra around the SH wavelength in 1DNPC composed of WSe_2 contains: N = 10, N = 20 segments.

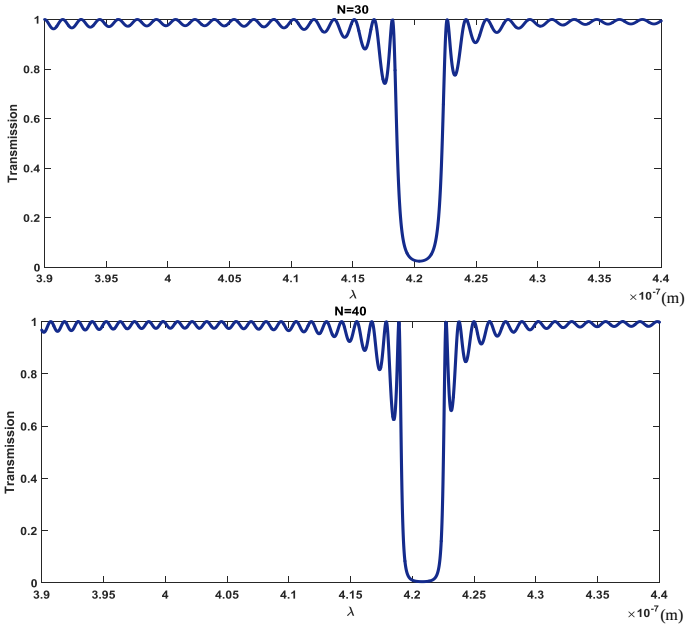

Fig. 18. Transmission spectra around the SH wavelength in 1DNPC composed of WSe_2 contains: N = 30, N = 40 segments.

In the structures shown in Figures 10-14 (1DNPC composed of WS_2) and according to the transmission coefficients versus wavelengths in the vicinity of FW and SH wavelength, the width of the gap decreases with increasing the number of layers: for N = 10, the width of the gap is about $10\mu m$ for FW and $2\mu m$ for SH wavelength, which this width for N=100 decreases to about $5\mu m$ for FW and about $1\mu m$ for SH wavelength. Also, the gap in the vicinity SH wavelength is narrower than that of FW wavelength. In the same manner, in the structures exhibited in Figures 15-18 (1DNPC composed of WSe_2), according to the transmission coefficients versus wavelengths in the vicinity of FW and SH wavelength, the width of the gap decreases with increasing number of layers: for N=10, the width of the gap is about $5\mu m$ for FW and $1\mu m$ for SH wavelength, which this width for N=40 decreases to about $1\mu m$ for FW and about $0.25\mu m$ for SH wavelength.

We ultimately investigated the optimal structure to achieve the highest SHG efficiencies by calculating the η_F and η_B versus the segment numbers; the results are represented in Figure 19.

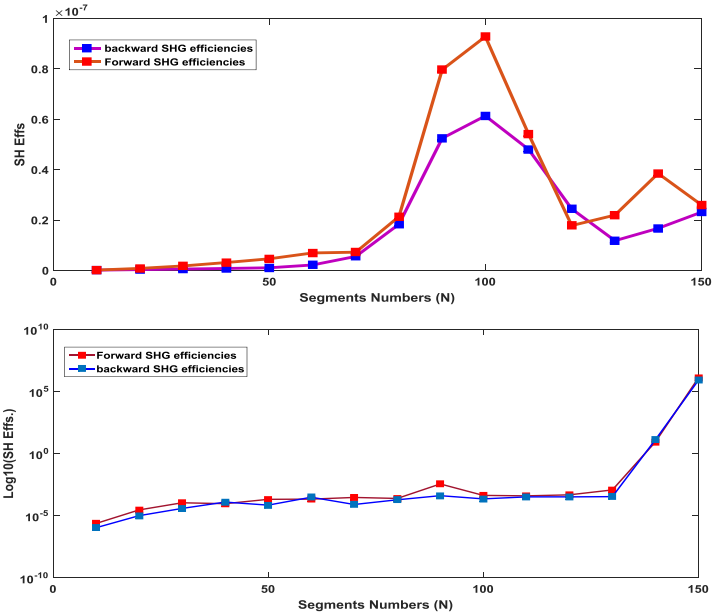

Fig. 19. Forward and backward SHG efficiencies versus the segment numbers for 1DNPC comprising of WS_2 (up) and WSe_2 (down).

The Figure shows the highest efficiencies for each structure containing different numbers of segments. As depicted in the Figure, the structure contains N = 100 segment (equal to N = 100 WS_2 monolayers) and has the highest SH efficiencies. Increasing the segment numbers above N = 100 diminished the SH efficiencies. We assume a fixed thickness for WS_2 monolayers ($d_{WS_2} = 61.8nm$) in the simulations. At low segment numbers, the sub-nanometer thickness of WS_2 monolayers had no significant effects on phase-matching conditions. Increasing the segment numbers enhanced the overall thickness (and optical path length of SH wave) of 2D nonlinear layers that affected the phase matching conditions and decreased the SH efficiencies. For 1DNPC comprising of WSe_2, SHG efficiencies increased uniformly with segment numbers (N). Also, there was no maximum point for a particular segment numbers. In this structure, the values of

forward and backward SHG efficiencies for each segment numbers are close together.

4. CONCLUSION

The SHG efficiencies from finite 1D photonic crystal containing 2DTMDC monolayers (as a 2D transient metal dichalcogenide structures), air, and SiO_2 films were calculated. We used the TMM in undepleted pump approximation for calculating the forward and backward SHG efficiencies. The results showed that the highest enhancement of SHG efficiencies up to three orders of magnitude in 1D photonic crystals contains sub wavelength WS_2 and WSe_2 monolayers including N = 10 and N=20 segments, respectively. The results also demonstrated about five orders of magnitude for N = 40 segments with respect to N = 1 for forward and backward efficiencies and about four orders of magnitude for N = 40 segments with respect to N = 1 for forward and backward efficiencies. Based on our observations, two and three orders of magnitude in 1D photonic crystals contains sub wavelength WS_2 (N = 10 segments) and WSe_2 (N=20 segments), respectively. The results can be obtained by carefully tuning the thickness of air and SiO_2 layers to meet the phase matching conditions.

References

[1] M. ZekavatFetrat, M. Sabaeian G. Solookinejad,, *The effect of ambient temperature on the linear and nonlinear optical properties of truncated pyramidal-shaped InAs/GaAs quantum dot* ,Journal of Optoelectronical Nanostructures (JOPN), 6 (3) (2021) 81-92. https://doi.org/10.30495/JOPN.2021.29138.1240

[2] G. Liang, X. Yu, X. Hu, B. Qiang, C. Wang, QJ WANG, *Mid-infrared photonics and optoelectronics in 2D materials*, Materials Today, 51 (2021) 294-316. https://doi.org/10.1016/j.mattod.2021.09.021

[3] A. Granados del Águila, S. Liu, T. TH Do, Z. Lai, TH. Tran, *Linearly Polarized Luminescence of Atomically-Thin MoS_2 Semiconductor Nanocrystals*, ACS Nano, 13 (11) (2019) 13006-13014. https://doi.org/10.1021/acsnano.9b05656

[4] C. Hou, J. Deng, J. Guan, Q. Yang, Z. Yu, Y. Lu, *Photoluminescence of Monolayer MoS_2 Modulated by Water/O2/Laser Irradiation*, Physical Chemistry Chemical Physics, 23(43) (2021) 24579-24588. https://doi.org/10.1039/D1CP03651C

[5] M. Wu, Y. Xiao, Y. Zeng, Y. Zhou, X. Zeng, L. Zhang, *Synthesis of two- dimensional transition metal dichalcogenides for electronics and optoelectronics*, InfoMat 3(4) (2021) 362-396 . https://doi.org/10.1002/inf2.12161

[6] W. Jin, P.-C. Yeh, N. Zaki, D. Zhang, J. T. Sadowski, A. Al- Mahboob, A. M. van Der Zande, D. A. Chenet, J. I. Dadap, I. P. Herman et al, *Direct measurement of the thickness-dependent electronic band structure of MoS2 using angle-resolved photoemission spectroscopy*, Phys. Rev. Lett. 111(10) (2013) 106801. https://doi.org/10.1103/PhysRevLett.111.106801

[7] Z. Sun, A. Martinez, and F. WANG, *Optical modulators with 2D layered materials*, Nature Photonics, *10*(4) (2016) 227-238. https://doi.org/ 10.1038/nphoton.2016.15

[8] L. Mennel, M. Paur, T. Mueller, *Second harmonic generation in strained transition metal dichalcogenide monolayers: MoS_2, $MoSe_2$, WS_2, and WSe_2*, APL Photonics 4(3) (2019) 034404. https://doi.org/10.1063/1.5051965

[9] Autere, A., Jussila, H., Dai, Y., Wang, Y., Lipsanen, H., & Sun, Z., *Nonlinear optics with 2D layered materials*, Advanced Materials, 30(24) (2018) 1705963. https://doi.org/10.1002/adma.201705963

[10] N. An, T. Tan, Z. Peng, C. Qin, Z. Yuan, L. Bi, C. Liao, *Electrically Tunable Four-Wave-Mixing in Graphene Heterogeneous Fiber for Individual Gas Molecule Detection*, Nano Lett., 20(9) (2020) 6473-6480. https://doi.org/10.1002/adma.201705963

[11] M. hasani, R. chegell, *Electronic and Optical Properties of the Graphene and Boron Nitride Nanoribbons in Presence of the Electric Field* , Journal of Optoelectronical Nanostructures (JOPN), 5(2) (2020) 49-64 .

https://doi.org/ 20.1001.1.24237361.2020.5.2.5.2

[12] S. Li, Y.-C. Lin, W. Zhao, J. Wu, Z. Wang, Z. Hu, Y. Shen, D.-M. Tang, J. Wang, Q. Zhang, H. Zhu, L. Chu, W. Zhao, C. Liu, Z. Sun, T. Taniguchi, M. Osada, W. Chen, Q.-H. Xu, A. T. S. Wee, K. Suenaga, F. Ding, and G. Eda, *Vapour-liquid-solid growth of monolayer MoS_2 nanoribbons*, Nature materials, 17 (6) (2018) 535-542.
https://doi.org/ 10.1038/s41563-018-0055-z

[13] X. Yang, Z. Sun, T. Low, H. Hu, X. Guo, F. J. García de Abajo, P. Avouris, and Q. Dai, *Nanomaterial-Based Plasmon-Enhanced Infrared Spectroscopy*, Advanced Materials 30(20) (2018) 1704896.
https://doi.org/ 10.1002/adma.201704896

[14] Z. Sun, *Electrically tuned nonlinearity*, Nature Photonics, 12(7) (2018) 383-385.
https://doi.org/ 10.1038/s41566-018-0201-9

[15] H. Chen, V. Corboliou, A. S. Solntsev, D.-Y. Choi, M. A. Vincenti, D. de Ceglia, C. de Angelis, Y. Lu, and D. N. Neshev, *Enhanced second-harmonic generation from two-dimensional $MoSe_2$ on a silicon waveguide*, Light: Science & Applications, 6(10) (2017) e17060-e17060.
https://doi.org/ 10.1038/lsa.2017.60

[16] M. Olyaee, M. Tavakoli , A. Mokhtari, Propose, *Analysis and Simulation of an All Optical Full Adder Based on Plasmonic Waves using Metal-Insulator-Metal Waveguide Structure*, Journal of Optoelectronical Nanostructures (JOPN), 4 (3) (2019) 95-116 .
https://doi.org/ 20.1001.1.24237361.2019.4.3.7.9

[17] Q. Leng, H. Su, J. Liu, L. Zhou, K. Qin, Q. Wang, J. Fu, *Enhanced second-harmonic generation in monolayer MoS_2 on suspended metallic nanostructures by plasmonic resonances*, Nanophotonics 10(7) (2021) 1871-1877.

https://doi.org/10.1515/nanoph-2021-0030

[18] K.-I. Lin, Y.-H. Ho, S.-B. Liu, J.-J. Ciou, B.-T. Huang, C. Chen, H.-C. Chang, C.-L. Tu, and C.-H. Chen, *Atom-Dependent Edge-Enhanced*

Second-Harmonic Generation on MoS_2 Monolayers, Nano Lett. ,18(2) (2018) 793-797.
https://doi.org/ 10.1021/acs.nanolett.7b04006

[19] C. T. Le, D. J. Clark, F. Ullah, V. Senthilkumar, J. I. Jang, Y. Sim, M.-J. Seong, K.-H. Chung, H. Park, and Y. S. Kim, Ann, *Nonlinear optical characteristics of monolayer $MoSe_2$*, Phys. 528 (7-8) (2016) 551-559.
https://doi.org/ 10.1002/andp.201600006

[20] NA. Pike, R. Pachter, *Second-Order Nonlinear Optical Properties of Monolayer Transition-Metal Dichalcogenides by Computational Analysis*, J. Phys. Chem. C, 125(20), 20 (2021) 11075-11084.
https://doi.org/ 10.1021/acs.jpcc.1c02380

[21] H. Zeng, G.-B. Liu, J. Dai, Y. Yan, B. Zhu, R. He, L. Xie, S. Xu, X. Chen, and W. Yao, *Optical signature of symmetry variations and spin-valley coupling in atomically thin tungsten dichalcogenides*, Sci. Rep. 3 (1) (2013) 1-5. https://doi.org/ 10.1038/srep01608

[22] A. V. Pakhomov, M. Hammerschmidt, S. Burger, T. Pertsch, and F. Setzpfandt, *Modeling of surface-induced second-harmonic generation from multilayer structures by transfer matrix method*, Optics Express, 29(6) (2021) 9098-9122.
https://doi.org/ 10.1364/OE.417066

[23] L .Peng, L. Hong, Z. Li ,*Theoretical solution of second-harmonic generation in periodically poled lithium niobate and chirped periodically poled lithium niobate thin film via quasi-phase-matching*, Phys. Rev. A, 104 (5) (2021), 053503.
https://doi.org/10.1103/PhysRevA.104.053503

[24] A. Gharaati , N. Miri , Z. Zareian, *Investigation and Comparison of Light Propagation in Two Graded Photonic Crystal Structures*, Journal of Optoelectronical Nanostructures (JOPN), 2 (1) (2017) 49-58.
https://doi.org/20.1001.1.24237361.2017.2.1.6.0

[25]. Hamidi, S. M., T. Parvini, and M. M. Tehranchi, *Efficient second harmonic conversion efficiency through one-dimensional coupled resonator poled nonlinear optical waveguide*, Applied Physics A, 111(2) (2013) 525-529. https://doi.org/10.1007/s00339-013-7599-1

[26]. K. Sakoda, Optical Properties of Photonic Crystals, 2nd edition, Springer Science & Business Media (2004). https://doi.org/10.1007/b138376

[27]. J.D. Joannopoulos, s.G. Johnson, J.N. Winn, R.D. Meade, Photonic crystals: molding the flow of light, Princeton University Press, Princeton, NJ (2011). https://doi.org/10.2307/j.ctvcm4gz9

[28]. C.M. Soukoulis, *Photonic crystals and light localization in the 21st century*, Springer Science and Business Media, Berlin (2012). https://doi.org/10.1007/978-94-010-0738-2

[29] http://sciencenotes.org/printable-periodic-table-chart-2015.

[30] M. K. Momma and F. Izumi, *VESTA 3 for three-dimensional visualization of crystal, volumetric and morphology data,* Journal of applied crystallography, 44 (6) (2011) 1272-1276. https://doi.org/10.1107/S0021889811038970

[31] Y. Li, A. Chernikov, X. Zhang, A. Rigosi, H. M. Hill, A. M. van der Zande, D. A. Chenet, E.M. Shih, J. Hone, and T. F. Heinz, *Measurement of the optical dielectric function of monolayer transition-metal dichalcogenides: MoS2, MoSe2, WS2, and WSe2* , Phys. Rev. B ,90 (20) (2014) 205422. https://doi.org/10.1103/PhysRevB.90.205422

[32] G. Ghosh, *Dispersion-equation coefficients for the refractive index and birefringence of calcite and quartz crystals*, Optics communications, 163(1-3) (1999) 95-102. https://doi.org/ 10.1016/S0030-4018(99)00091-7

[33] A. Kumar, V. Kumar, A. Nautiyal, K.S. Singh, S.P. Ojha, *Optical switch based on nonlinear one dimensional photonic band gap materia*, Optik, 145 (2017) 473-478. https://doi.org/_10.1016/j.ijleo.2017.07.062

[34] O. Bahrami, A. Baharvand, *Nonlinear Optical Effects in One Dimensional Multi-Layer Structure Consisting of Polar Ferroelectric Called* $LiTaO_3$, Journal of Optoelectronical Nanostructures (JOPN), 6 (1) (2021) 21-34. https://doi.org/10.30495/JOPN.2021.4539